Strong local lattice instability in hexagonal ferrites $R\mathrm{Fe_2O_4}$ (R = Lu,Y,Yb) revealed by x-ray absorption spectroscopy

Sara Lafuerza,[1,*] Joaquín García,[1] Gloria Subías,[1] Javier Blasco,[1] and Vera Cuartero[2]

[1]*Instituto de Ciencia de Materiales de Aragón, Departamento de Física de la Materia Condensada, CSIC-Universidad de Zaragoza, Zaragoza, 50009, Spain*

[2]*ALBA Synchrotron Radiation Facility, Ctra. BP1413 km 3.3, 08290 Cerdanyola del Vallès, Barcelona, Spain*

(Received 14 October 2013; revised manuscript received 13 December 2013; published 22 January 2014)

We present here an x-ray absorption study of the $R\mathrm{Fe_2O_4}$ series ($\mathrm{LuFe_2O_4}$, $\mathrm{YFe_2O_4}$, $\mathrm{YbFe_2O_4}$, and $\mathrm{LuCoFeO_4}$) at the Fe K-edge. Extended x-ray absorption fine structure (EXAFS) and x-ray absorption near-edge structure (XANES) spectra were measured at temperatures ranging from 100 K to 390 K crossing the charge ordering (CO) transition temperatures on both isotropic and oriented powder samples. Unpolarized and polarized x-ray absorption spectra with the x-ray polarization parallel and perpendicular to the hexagonal c axis were obtained separately. The XANES spectra show almost no dependence with either polarization or temperature. This indicates that, in contrast to its average crystallographic structure, the local electronic and geometrical state of the Fe atom is barely anisotropic, and it remains the same above and below the proposed CO. Moreover, the linear combination of two spectra corresponding to the pure ionic states Fe^{2+} and Fe^{3+} does not fit to the experimental XANES of either $\mathrm{LuFe_2O_4}$, $\mathrm{YFe_2O_4}$, or $\mathrm{YbFe_2O_4}$, discarding total ionic segregation in favor of an intermediate mixed valence state. The maximum charge disproportionation compatible with the XANES spectra is 0.5 ± 0.1 electrons in the whole temperature range. The polarized EXAFS spectra have allowed us to analyze the local structure separating the different contributions mixed up in the polycrystal. Best-fit results show that the five oxygen atoms of the first coordination shell are at nearly the same distance but with a large Debye-Waller factor. Neither the interatomic distances nor the Debye-Waller factors of the first oxygen coordination shell change with temperature, indicating that the dynamical structural distortion of the high-temperature symmetric hexagonal phase freezes upon cooling down. Thus, the local structure instability of the mixed valence is in the origin of the structural transitions.

DOI: 10.1103/PhysRevB.89.045129 PACS number(s): 61.05.cj, 78.70.Dm, 71.30.+h, 72.80.Sk

I. INTRODUCTION

Hexagonal ferrites $R\mathrm{Fe_2O_4}$ have been a matter of deep study in the past [1,2] but also recently in the search for multiferroic materials [3,4]. The crystal structure of these compounds belongs to the rhombohedral system with space group R-3m [5,6]. In the equivalent hexagonal setting, it can be described along the c axis as a stacking of $[\mathrm{Fe_2O_4}]_\infty$ bilayers, each consisting of two triangular $[\mathrm{FeO}]_\infty$ planes, separated by close-compact $[\mathrm{RO_2}]_\infty$ layers. The formal valence of the Fe ions is then 2.5 as determined from single-electron counting.

These compounds show different phase transitions coincident with structural changes whose origin was ascribed to the mixed valence state of the iron ion. Despite the $R\mathrm{Fe_2O_4}$ oxides having the same crystallographic structure at temperatures above the phase transitions, the physical properties vary depending on the rare earth atom. $\mathrm{LuFe_2O_4}$ is the most studied member of this family, since it was proposed to be a multiferroic material [7]. The occurrence of ferroelectricity below 320 K and ferrimagnetism at 240 K would make this compound very interesting due to the possible coupling between these two degrees of freedom [8]. On heating, $\mathrm{YFe_2O_4}$ shows two metal-insulator transitions at $T_N \sim 240$ K and $T_L \sim 220$ K that are accompanied by crystal distortions to monoclinic and triclinic, respectively, and below T_N the iron ions couple antiferrimagnetically [1,9,10]. These transitions show a large thermal hysteresis, and the temperatures shift to $T_N \sim 230$ K and $T_L \sim 180$ K on cooling. Finally, $\mathrm{YbFe_2O_4}$ behaves like a bad insulator with a resistivity that increases upon lowering the temperature and shows magnetic ordering below $T_N \sim 240$ K [11].

Both the metal-insulator phase transitions in $\mathrm{YFe_2O_4}$ and the ferroelectricity in $\mathrm{LuFe_2O_4}$ have been explained as originating from charge ordering (CO), i.e., electronic localization giving rise to a Fe^{3+} and Fe^{2+} ionic ordering in the hexagonal lattice. In the case of $\mathrm{YFe_2O_4}$, where ferroelectricity was not postulated, the transitions were classified as Verwey-type due to its similarity with the metal-insulator transition in $\mathrm{Fe_3O_4}$ [12], for which the octahedral iron atoms also have a formal valence of 2.5. Verwey proposed that above T_{CO} the extra electron is free to jump between different iron sites, giving electrical conduction. Below T_{CO} this electron is localized on the iron sites, impeding its mobility. However, it has been later demonstrated that this Verwey CO model is at odds with the experimental facts in $\mathrm{Fe_3O_4}$ because the charge distribution is not bimodal and the maximum charge disproportionation found is much lower than one electron [13,14]. On the other hand, the CO transition in $\mathrm{LuFe_2O_4}$ was considered to originate electrical dipoles in the geometrically frustrated triangular Fe lattice that would give rise to ferroelectricity [15]. For $\mathrm{YbFe_2O_4}$, also thought to be a candidate for multiferroicity, an incommensurate CO ordering has been proposed to occur below $T_{CO} = 305$ K [16]. Remarkably, no sharp discontinuities like those in $\mathrm{YFe_2O_4}$ are observed in the electrical conductivity at the CO transition in either $\mathrm{LuFe_2O_4}$ or $\mathrm{YbFe_2O_4}$ [17].

Although a large number of papers have been published trying to explain the mechanism of multiferroicity originating

*lafuerza@unizar.es

from CO in $LuFe_2O_4$ [3,15,18–36], recent experimental works indicate that it is not ferroelectric. On one hand, the claimed colossal dielectric constants are spurious effects originating from the electrical contacts [37–39], and on the other hand, $LuFe_2O_4$ does not show spontaneous electrical polarization, as has been proved by electrical polarization measurements [39]. Although the occurrence of ferroelectricity can be discarded in $LuFe_2O_4$, the structural phase transition at $T_{CO} \approx 320$ K is still considered to originate from Fe^{3+}/Fe^{2+} CO. Resonant x-ray scattering (RXS) experiments at the Fe K-edge of the principal observed superstructure (1/3, 1/3, half-integer) reflections seem to support this assumption, but the analysis performed by either Ikeda *et al.* [7] or Mulders *et al.* [40] are merely qualitative, using a generic structure factor without considering any charge order sequence. Other authors have shown that the CO involves charged, rather than polar, bilayers with four different iron valences, but with values that are still grouped in a bimodal distribution of two different iron atoms, referred as Fe^{3+}- and Fe^{2+}-like [27].

X-ray absorption spectroscopy (XAS) at the transition-metal ($3d$) K-edges has been important in elucidating charge disproportionation and local structural changes in many mixed-valence transition-metal compounds displaying CO. The ability to determine the valence state results from two facts: the XAS spectrum of a sample with mixed chemical species corresponds to the incoherent addition of the individual XAS spectra of each species, and the x-ray absorption near-edge structure (XANES) region of the XAS spectrum is strongly sensitive to the formal oxidation state of the absorbing atom. The main absorption edge in the XANES spectrum shifts to higher energy with increasing oxidation state (chemical shift) [41]. Because of this chemical shift of some few electron volts between different ionic states, Mn K-edge and Fe K-edge XANES have been successfully used to demonstrate the absence of a bimodal distribution of either Mn^{3+} and Mn^{4+} ions in manganites [42] or Fe^{3+} and Fe^{5+} ions in the $La_{1-x}Sr_xFeO_3$ series [43], respectively. Moreover, the extended part of the XAS spectra [i.e. extended x-ray absorption fine structure (EXAFS)] provides geometrical information on the neighboring atoms surrounding the transition-metal atom in a time scale shorter than that of lattice vibrations. Consequently, EXAFS can distinguish thermal and structural disorder in the local structure and has been fundamental to determining the order-disorder structural character of most of the so-called CO transitions in the mixed-valence transition-metal compounds [43–45].

This background motivates the present Fe K-edge XAS study across the CO transitions in the mixed-valence RFe_2O_4 compounds: $LuFe_2O_4$, YFe_2O_4, and $YbFe_2O_4$. In addition, the hexagonal ferrite $LuFeCoO_4$ with nominal iron valence Fe^{3+} also has been studied as a reference compound. The polarization-dependent XAS enables us to explore the anisotropy in the local electronic structure around the iron atoms, as well as better resolve the contributions coming from the different coordination shells. The temperature dependence of the XANES and EXAFS spectra allows us to determine changes in the Fe valence state and in the local structure disorder, respectively, when crossing the different phase transitions. Our results show the absence of a bimodal distribution of Fe^{3+}/Fe^{2+}, limiting the maximum charge disproportionation to about 0.5 ± 0.1 electrons. On the other hand, a strong dispersion on the Fe-O interatomic distances is observed at all temperatures only in the mixed-valence RFe_2O_4 compounds, indicating the presence of strong local structure instability that is at the origin of the so-called CO transitions reported for these ferrites.

II. EXPERIMENTAL

Polycrystalline powders of RFe_2O_4 (R = Lu,Y,Yb) were obtained by solid state chemistry reaction from stoichiometric amounts of R_2O_3 and Fe_2O_3 and sintered at 1200 °C (R = Lu,Yb) and 1240 °C (R = Y) in a CO_2/CO (60:40) atmosphere. Similarly, $LuFeCoO_4$ powder samples were prepared in air at 1350 °C using Lu_2O_3, Fe_2O_3, and CoO as precursors. The obtained specimens were single phase, as checked by conventional powder x-ray diffraction (XRD). Differential scanning calorimetry (DSC) measurements were performed for comparison with previous reports in literature [9,38] and to check the quality of the samples. Figure 1 shows the temperature-dependent heat capacity of the three studied RFe_2O_4 (R = Lu,Y,Yb) samples, where anomalies originated by the different CO and magnetic phase transitions are observed at temperatures close to those expected for stoichiometric samples.

Highly oriented pellets were obtained by mixing the polycrystalline powders with an epoxy resin and then allowing the mixture to solidify in a magnetic field of about 1 tesla at room temperature. After this process, the resulting pellet became oriented with the hexagonal c axis parallel to the magnetic field. Following this procedure, two different types of oriented pellets were prepared having the c axis either within or normal to the pellet surface. Figure 2 compares the XRD patterns of isotropic $LuFe_2O_4$ and an oriented pellet with the c axis normal to the pellet surface. We observe that only peaks associated with the (00l) reflections are seen in the oriented sample, guaranteeing a degree of orientation greater than 99%.

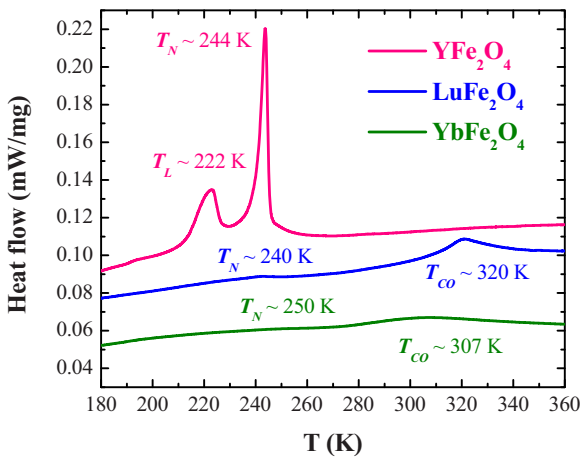

FIG. 1. (Color online) DSC measurements (heating runs) for powder samples of RFe_2O_4 (R = Lu,Y,Yb). Phase transitions temperatures determined from the anomalies in the heat capacity curves are indicated.

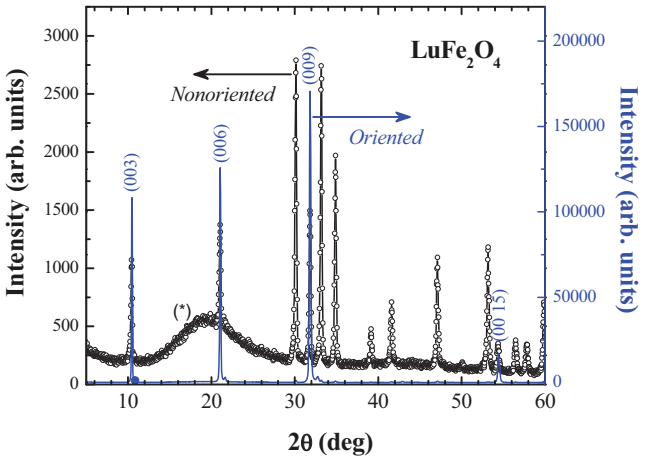

FIG. 2. (Color online) X-ray diffraction patterns at room temperature for pellets of $LuFe_2O_4$ powder mixed with araldite: nonoriented and oriented with the c axis perpendicular to the pellet plane (i.e., parallel to the scattering vector). Asterisk marks the contribution from amorphous araldite noticeable in the nonoriented pellet. For the oriented sample, a high degree of orientation is obtained and only the (00l) reflections appear.

XAS measurements were carried out at beamline BL22-CLAESS [46] of the ALBA synchrotron radiation facility. The incident beam was defocused to give a spot size of H × V ∼ 1.5 × 0.7 mm^2, allowing averaging of a big sample area. A Si(111) double-crystal monochromator was used, although the Si(311) double-crystal monochromator was also checked with no appreciable differences in the spectral features. The quick energy-scanning mode was employed for recording the spectra with typical acquisition time per point of about 0.5 s. XANES and EXAFS spectra were recorded at the Fe K-edge (7112 eV) in transmission mode using ionization chambers as detectors. An iron foil was measured simultaneously for energy calibration. XAS measurements were performed at temperatures ranging from about 100 K to 390 K using a liquid nitrogen cryostat. On one hand, nonpolarized XAS measurements were undertaken on pellets of powder samples prepared by dilution with cellulose to get a jump at the edge of about 1. On the other hand, polarized XAS spectra were measured on the oriented pellets with the x-ray polarization vector **E** parallel and perpendicular to the hexagonal c axis. The thickness of the oriented pellets was also optimized to get a good signal to noise ratio. Additionally, XAS measurements as a function of temperature on pellets of polycrystalline $LuFe_2O_4$ (187–290 K), YFe_2O_4 (160–265 K), and $LuCoFeO_4$ were also performed in transmission at the SAMBA beamline of the SOLEIL synchrotron. In this case, a Si(220) double-crystal monochromator was used, and the spectra were also recorded in the quick energy scanning mode [47]. Both XANES and EXAFS unpolarized spectra were equal to those measured at CLAESS. XANES spectra were normalized by first subtracting the linear pre-edge contribution and fixing the jump to 1 at values well above the absorption edge. The Fourier transforms (FTs) of the EXAFS signals were calculated for a k-range typically of 1.5–12 $Å^{-1}$ using a sine window. The EXAFS structural analysis was performed using theoretical phases and amplitudes calculated by the FEFF-6 code [48], and fits to the experimental data were carried out in R-space with the ARTEMIS program (version 0.8.12) of the IFFEFIT package [49].

III. RESULTS

A. XANES spectra

Figure 3(a) shows normalized Fe K-edge XANES spectra of the mixed-valence RFe_2O_4 (R = Lu,Y,Yb) and $LuFeCoO_4$ compounds recorded at room temperature for the two orientations between the polarization vector **E** and the crystallographic c axis (**E//c** and **E⊥c**). The first derivatives of the spectra are plotted in Fig. 3(b). The nonpolarized spectra have been also included showing good agreement with the weighted addition (1/3)**E//c** + (2/3)**E⊥c**. We first note the strong similarity in the spectral line shape of the nonpolarized XANES among the different compounds including $LuFeCoO_4$, where the iron atom has formal valence 3+. The major difference is the energy position of the main absorption edge. The latter is identical for the mixed-valence

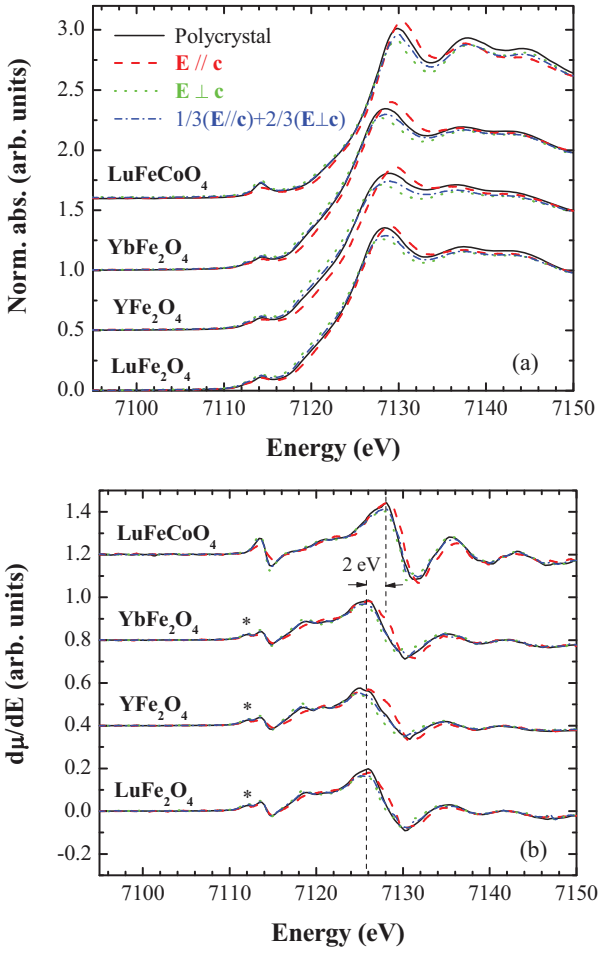

FIG. 3. (Color online) (a) Normalized XANES spectra at room temperature for the $LuFe_2O_4$, YFe_2O_4, $YbFe_2O_4$, and $LuFeCoO_4$ samples: nonpolarized (solid), polarized **E//c** (dash), **E⊥c** (dot), and weighted addition 1/3**E//c** + 2/3**E⊥c** (dash dot). The spectra are shifted in vertical for clarity. (b) First derivative of the above absorption spectra for the same samples.

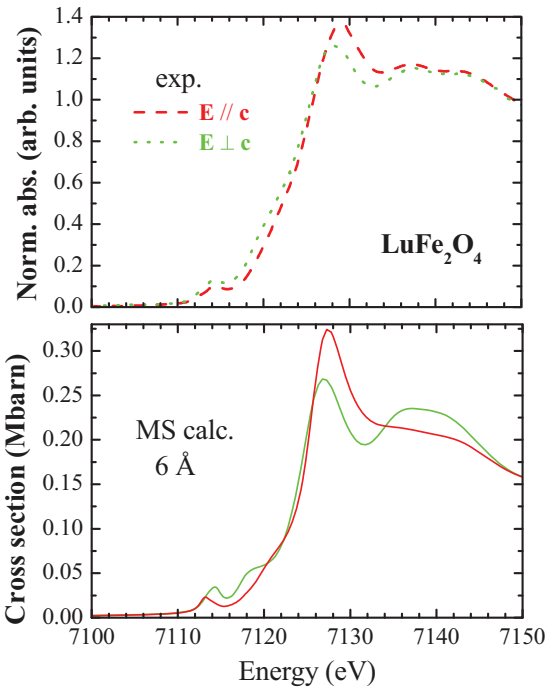

FIG. 4. (Color online) Comparison between experimental polarized XANES spectra at the Fe K-edge of $LuFe_2O_4$ for **E//c** and **E⊥c** (top panel) and the corresponding multiple scattering (MS) theoretical absorption calculations (bottom panel) obtained for a cluster of 6 Å around the Fe atom (about 70 atoms) in the hexagonal structure.

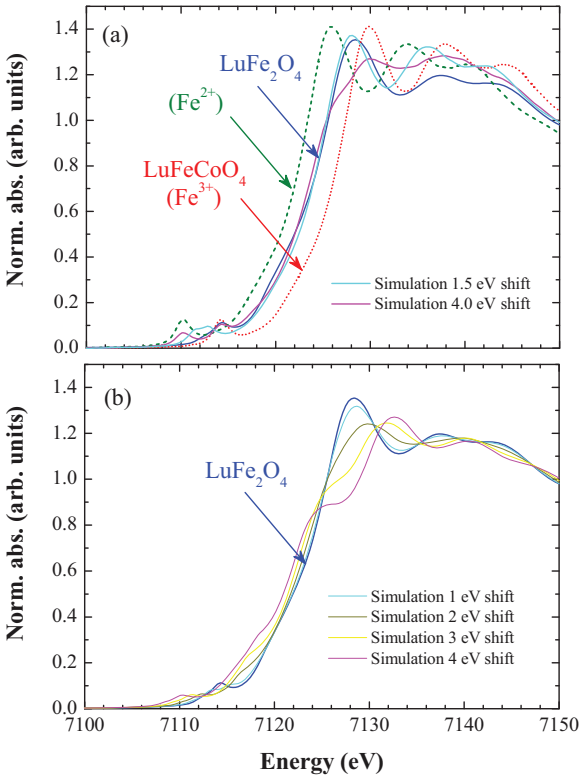

FIG. 5. (Color online) Nonpolarized XANES spectrum of $LuFe_2O_4$ compared with the simulated spectra obtained by 50%:50% weighted addition of the XANES spectra corresponding to $Fe^{(2.5+\delta)+}$ and $Fe^{(2.5-\delta)+}$ valence states using $LuFeCoO_4$ (panel a) and $LuFe_2O_4$ (panel b) as reference for the hexagonal local structure. The XANES spectra for the $Fe^{(2.5+\delta)+}$ and $Fe^{(2.5-\delta)+}$ valence states are obtained shifting the edge energy by $\pm\Delta E = 4\delta$ eV, respectively.

RFe_2O_4 samples, as expected from the same formal valence state 2.5+, but it is shifted by about 2 eV to higher energy for $LuFeCoO_4$, as is deduced from the maximum of the derivative spectra in Fig. 3(b). The other clear difference is the presence of a distinct feature at the pre-edge located around 7112 eV in all the mixed-valence RFe_2O_4 compounds [marked by an asterisk in Fig. 3(b)], which is absent in $LuFeCoO_4$. Only the feature located at 7114 eV is present for all the studied ferrites. We assign the two peaks to the $3d^5$ and $3d^6$ configurations of the mixed valence iron state. The Fe in the hexagonal RFe_2O_4 ferrites is surrounded by an oxygen bipyramid of triangular basis with three oxygen atoms ($d_{\text{Fe-Obasal}} = 2.00$ Å) located in the ab plane and one above ($d_{\text{Fe-O1ap}} = 1.95$ Å) and one below ($d_{\text{Fe-O2ap}} = 2.2$ Å) along the c axis [5,6]. Thus, the polarized **E⊥c** and **E//c** XANES spectra represent the projected density of empty p states in the basis and along the axis of the bipyramid, respectively. Although the FeO_5 local structure is strongly anisotropic, the spectral line shape of the polarized **E//c** and **E⊥c** XANES is almost identical to each other, and there is almost no energy shift (<1 eV) between the two polarizations [Fig. 3(a)]. The main differences are found in the intensity of the pre-edge features and the white line. The prepeaks, characteristic of the quadrupolar $1s$-$3d$ transitions, are smaller for **E//c** than for **E⊥c**, but the opposite occurs for the white line resonance. This behavior is general for all the studied hexagonal ferrites, independent of both the type of R atom and the iron formal valence. In order to gain new insights into the polarization dependence of the XANES experimental spectra, we have carried out multiple-scattering (MS) simulations with polarization analysis, distinguishing contributions along and perpendicular to the hexagonal c axis for the $LuFe_2O_4$ compound. Theoretical calculations of the XANES spectra at the Fe K-edge of $LuFe_2O_4$ were performed using the FDMNES code [50] in the MS real-space approach within the muffin-tin (MT) approximation for the potential. The exchange–correlation part of the potential was taken as the real Hedin, Lundqvist, and Von Barth potential, and the spectra were convoluted using an appropriate Lorentzian function. The high-temperature rombohedral crystal structure of $LuFe_2O_4$ [6] was employed to obtain the atomic positions. Figure 4 compares the calculated XANES spectra obtained for a cluster radius of 6 Å around the Fe atom (about 70 atoms) to the corresponding experimental polarized XANES spectra for both, **E//c** and **E⊥c** polarizations. The simulated spectra nicely reproduce the minimal differences observed between the two polarized experimental spectra, confirming the lack of strong anisotropy in the local structure around the Fe atoms.

One of the key points in this study is to determine whether the proposed bimodal distribution Fe^{2+}/Fe^{3+} can describe the experimental XANES spectra. Since the phenomenology is identical for the three mixed-valence RFe_2O_4 (R = Lu,Y,Yb) compounds, we will focus the discussion exclusively on $LuFe_2O_4$ as the representative example. If there is coexistence of Fe^{2+} and Fe^{3+} valence states as in heterogeneous mixed-valence compounds, the XANES spectra of $LuFe_2O_4$ should

agree with the 1:1 addition of the individual XANES spectra of appropriate Fe^{3+} and Fe^{2+} reference compounds. For Fe^{3+}, the appropriate reference compound is LuFeCoO4, whereas for Fe^{2+}, it would be $LuFeGaO_4$ as reported by Ikeda [51]. However, our attempts to obtain it were unsuccessful, and we always found a mixture of phases, including $LuFe_2O_4$, in our specimens. Since the main difference between XANES spectra of different ionic states with similar local structure geometry (that is the FeO_5 bipyramid) comes from the chemical shift of the absorption edge, being that their spectral shape is alike because it mainly depends on the local structural geometry [52], we have performed two simulations. The first one uses the XANES spectra of $LuFeCoO_4$ as reference for the hexagonal (space group R-3m) structure, while the second one makes use of the $LuFe_2O_4$ XANES spectra. This approach is particularly accurate at the energy region of the rising edge where the absorption cross section monotonously increases. In the first case, we have taken as reference of Fe^{2+} the $LuFeCoO_4$ (Fe^{3+}) spectrum shifted by $2\Delta E = 1.5$ and 4 eV (chemical shift between Fe^{2+} and Fe^{3+} [41]). In the second case, the $LuFe_2O_4$ spectrum has been shifted symmetrically $\pm\Delta E = 0.5$, 1, 1.5, and 2 eV. Figure 5 shows the simulations resulting from the 1:1 linear combination of the XANES spectra of $LuFeCoO_4$ (panel a) and $LuFe_2O_4$ (panel b) as reference compounds for the different energy chemical shifts. A monotonous increase of the main absorption edge is expected for a single mixed-valence $Fe^{+2.5}$ state, whereas if two $Fe^{2.5+\delta}$ and $Fe^{2.5-\delta}$ valence states coexist with 2δ the charge disproportionation, the peak of the main absorption edge would broaden with increasing ΔE. We observe that the $LuFe_2O_4$ XANES spectrum disagrees with the simulations corresponding to chemical shifts of 3 and 4 eV, as they show a clear shoulder at the rising absorption edge and a decrease of the main peak. However, the difference between the simulated and experimental spectra is very small when we use a chemical shift of 1.5 ± 0.5 eV. Taking into account the linearity between formal valence and chemical shift [41] that one electron of charge disproportionation between Fe^{2+} and Fe^{3+} corresponds to a chemical shift of 4 eV, we can conclude that the maximum electronic disproportion between the different Fe atoms in the $LuFe_2O_4$ sample should be less than 0.5 electrons. This result implies the absence of ionic species Fe^{3+} and Fe^{2+} in the mixed-valence RFe_2O_4 ferrites but does not discard a multimodal distribution with a standard deviation less than 0.5 electrons. In the particular case of a bimodal distribution, the valence states for the Fe atoms will be $Fe^{2.25+}$ and $Fe^{2.75+}$. We conclude the same charge disproportionation for $YbFe_2O_4$ and YFe_2O_4 compounds since XANES spectra are almost like that of $LuFe_2O_4$, as shown in Fig. 3.

The XANES spectra of RFe_2O_4 were recorded at temperatures below and above the phase transitions without

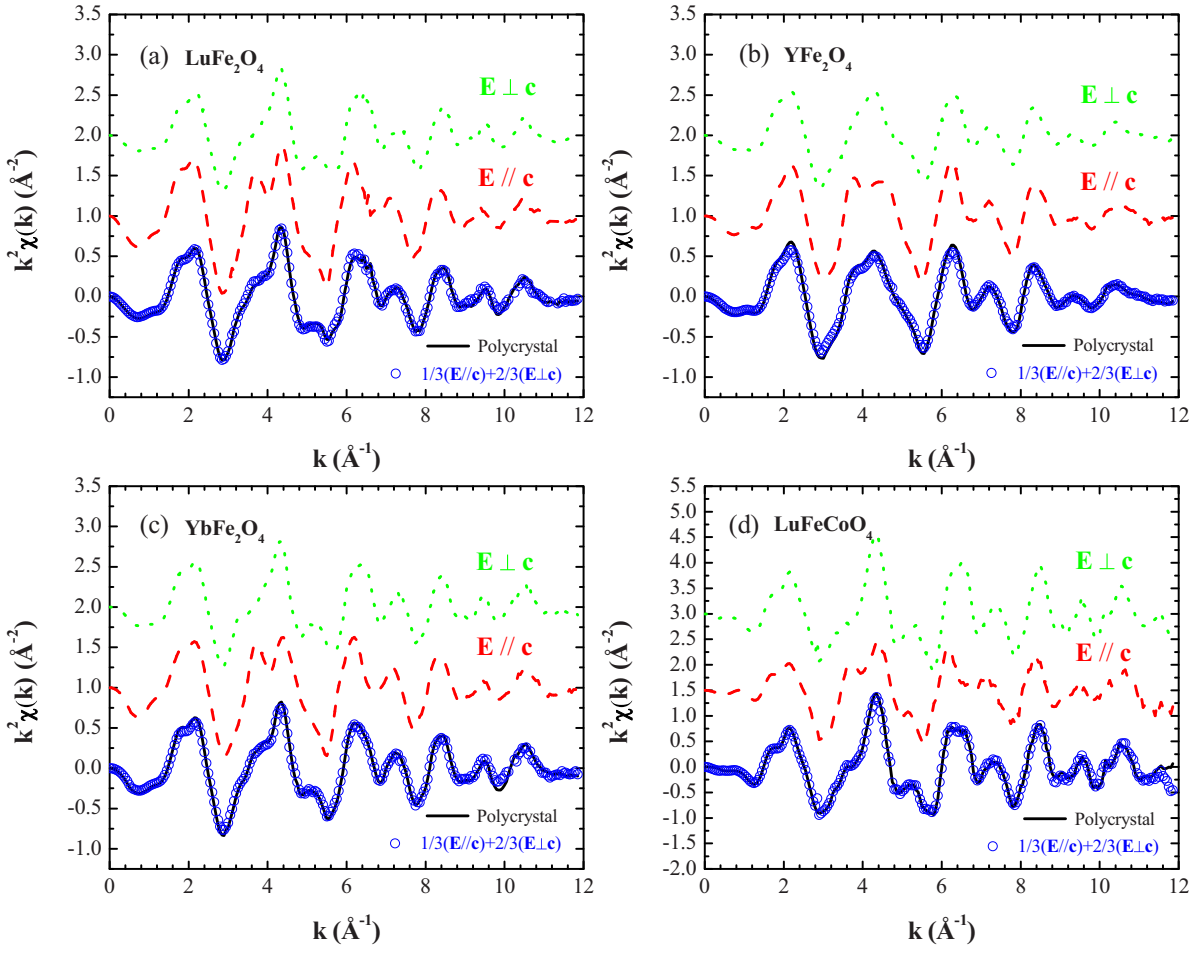

FIG. 6. (Color online) $k^2\chi(k)$ EXAFS signals at room temperature nonpolarized (solid), polarized **E//c** (dash), **E⊥c** (dot), and weighted addition $1/3$**E//c** $+ 2/3$**E⊥c** (circles) for: (a) $LuFe_2O_4$, (b) YFe_2O_4, (c) $YbFe_2O_4$, and (d) $LuFeCoO_4$ samples.

finding any changes. This fact means that the charge and geometrical distribution of the iron atoms in these compounds remains unaltered in the different phases. Due to the very short interaction time of the photoabsorption process, this can be explained by a dynamical distribution above the transition temperature and a static distribution below the so-called CO.

B. EXAFS spectra

Figure 6 presents the nonpolarized and polarized $k^2\chi(k)$ EXAFS signals for all the studied $R\mathrm{Fe_2O_4}$ ferrites recorded at room temperature. The addition $(1/3)\mathbf{E}//\mathbf{c} + (2/3)\mathbf{E}\perp\mathbf{c}$ of the $k^2\chi(k)$ signals, displayed together with the nonpolarized spectrum, perfectly agrees with it, demonstrating the coherence of the experiment. By displaying the modulus of the FTs of the EXAFS spectra, which provides a measure of the radial distribution function around the Fe atom, the differences among the compounds under study can be better elucidated. The comparison of the modulus of the FTs of the k^2-weighted EXAFS spectra for the polycrystalline samples of $\mathrm{LuFe_2O_4}$, $\mathrm{YFe_2O_4}$, $\mathrm{YbFe_2O_4}$, and $\mathrm{LuFeCoO_4}$ is shown in Fig. 7(a). The first main isolated peak corresponds to the first-neighbors coordination shell, which is a bipyramid with five oxygen atoms, three in the hexagonal equatorial plane and two along the crystallographic c axis. Following the main peak, a second structure is also observed between 2 and 4 Å, which includes mixed contributions from the next neighbors: Fe (Fe/Co in the $\mathrm{LuFeCoO_4}$ case), R (= Lu,Y,Yb), and second-shell oxygen atoms. The intensity of the FT is larger for the reference compound $\mathrm{LuFeCoO_4}$ compared with the mixed-valence $R\mathrm{Fe_2O_4}$ compounds. This fact indicates a more distorted local structure around the iron atom for the mixed-valence compounds, involving not only the first, but also further, coordination shells.

The polarized EXAFS spectra are very useful in this case to discriminate the individual contributions of each type of surrounding atoms that otherwise are overlapped in the nonpolarized data. As a matter of illustration, Fig. 7(b) shows the modulus of the FTs of the k-weighted EXAFS spectra for the two measured polarizations $\mathbf{E}//\mathbf{c}$ and $\mathbf{E}\perp\mathbf{c}$ compared with the modulus of the polycrystal for $\mathrm{LuFe_2O_4}$ at room temperature. It is clear from the polarized EXAFS data that the strong contribution from the Fe-$\mathrm{Fe}_{\perp c}$ pair within the hexagonal equatorial plane is suppressed in the $\mathbf{E}//\mathbf{c}$ FT spectrum, whereas the Fe-$\mathrm{Fe}_{//c}$ and Fe-$\mathrm{Lu}_{//c}$ apical bonds are mostly suppressed in $\mathbf{E}\perp\mathbf{c}$. For simplicity, we have adopted the hexagonal crystallographic structure (space group R-3m) common for all ferrites at high temperature to calculate theoretical amplitudes and phases for each scattering path up to 4.6 Å, including the first Fe-O and the second Fe-Fe(R) coordination shells. The polarized EXAFS spectra were then fit using the Artemis program [49] with effective fixed coordination numbers calculated, taking into account the angle between the x-ray polarization vector $\mathbf{E}$ and the position vector associated with the Fe bond with each neighboring atom j, $\mathbf{R}_j$ [53]. For the first coordination shell, this means that only the two apical oxygen atoms contribute to the $\mathbf{E}//\mathbf{c}$ spectra (bonds to the equatorial O atoms are orthogonal to $\mathbf{E}$) but with an effective coordination number $N_{\mathrm{eff}} = 6$ given

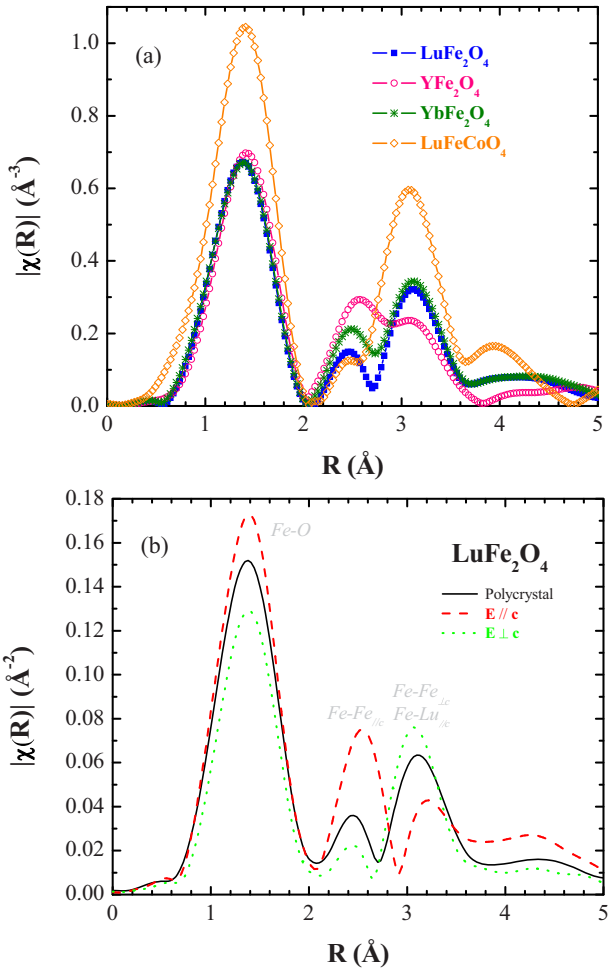

FIG. 7. (Color online) (a) Moduli of the FTs of the $k^2\chi(k)$ EXAFS signals for the polycrystalline samples of $\mathrm{LuFe_2O_4}$, $\mathrm{YFe_2O_4}$, $\mathrm{YbFe_2O_4}$, and $\mathrm{LuFeCoO_4}$ at room temperature. (b) Moduli of the FTs of the $k\chi(k)$ EXAFS signals for polycrystalline and oriented samples of $\mathrm{LuFe_2O_4}$ at room temperature.

by $N_{\mathrm{eff}} = N_j \times 3\cos^2\theta$, with θ the angle between the Fe-O bond vector and the crystallographic c axis. Correspondingly, only the three equatorial oxygen atoms contribute to the $\mathbf{E}\perp\mathbf{c}$ spectra with $N_{\mathrm{eff}} = 4.4$ given by $N_{\mathrm{eff}} = N_j \times 3/2\ \sin^2\theta$. The analysis procedure followed first fit the polarized EXAFS spectra and then simulated the nonpolarized spectrum with the structural parameters obtained in the previous fits to check the coherence of the method. The variables in the fits were the interatomic distances R_j and the Debye-Waller (DW) factors σ_j^2. The amplitude reduction factor S_0^2 was fixed to 0.7, the value obtained for the reference compound $\mathrm{LuFeCoO_4}$. The threshold energy E_0 was also permitted to vary in the fitting process, being very similar for the different samples and polarizations ($\Delta E_0 \approx 5$ eV). Figure 8 shows the comparison between best fit and experimental spectra for the polarized data and the resultant simulation of the nonpolarized spectrum compared with the polycrystal in terms of both the moduli of the FTs of the k-weighted EXAFS [Fig. 8(a)] and the Fourier-filtered spectra in k-space [Fig. 8(b)] for $\mathrm{LuFe_2O_4}$. Similar agreements were found for the other ferrites. The relevant structural parameters obtained for the different compounds

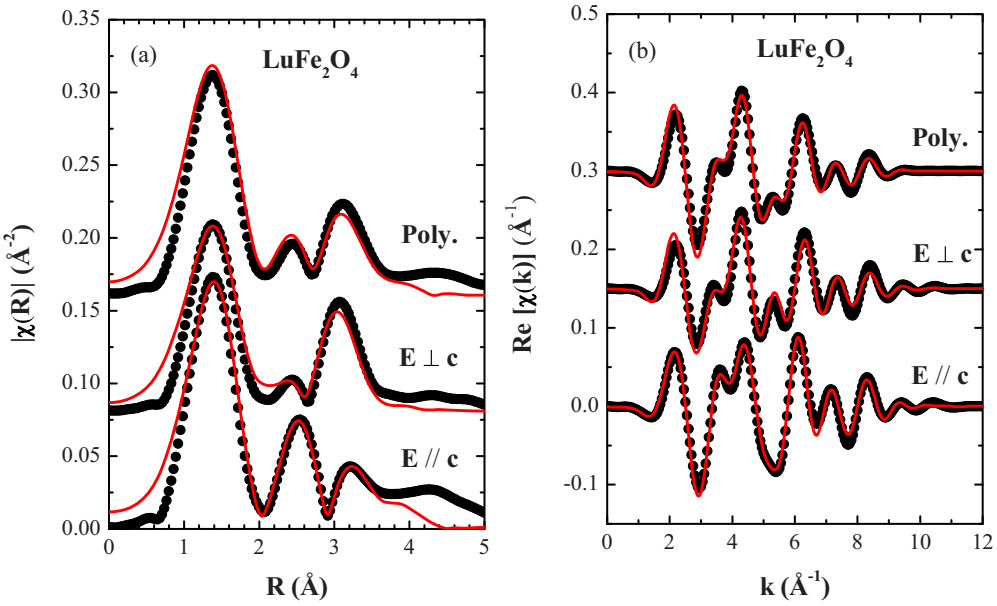

FIG. 8. (Color online) Comparison between experimental data (circles) and best fits (solid lines) for the polarized and nonpolarized spectra of $LuFe_2O_4$. (a) Moduli of the FTs of the $k\chi(k)$ EXAFS signals and (b) real part of the Fourier-filtered spectra in k-space.

at room temperature are given in Table I. We observe that the average Fe-O (apical) bonds of the FeO_5 bipyramids are significantly lower than the average crystallographic Fe-O distance (~2.08 Å) given for the hexagonal structure from diffraction studies [5,6], although it approaches the value of the shorter Fe-O bond along the c axis. However, the correspondingly high σ^2 factors indicate the presence of a spread of distances. Taking into account our experimental limitations, we cannot rule out the possibility of two distances with a maximum distortion of 0.1 Å. This distortion is also in contrast to the strong apical distortion of 0.25 Å obtained from crystallography for the hexagonal phase [5,6]. In the case of $LuFe_2O_4$, which is already in the CO monoclinic phase at room temperature, a plausible explanation could be the presence of different distortions along the c axis for the four distinct crystallographic Fe sites that results in a reduced average apical distortion. However, we note here that the discrepancy in the magnitude of the apical distortion between the EXAFS and the crystallographic data also occurs for all the remaining RFe_2O_4 ferrites, including the reference $LuFeCoO_4$ compound, which show the hexagonal crystallographic structure at room temperature. The presence of distortions is not expected in those cases. On the other hand, the average distances for the Fe-O (equatorial) bonds agree much better with those obtained from x-ray diffraction [5,6]. Regarding the σ^2 factors, they are anomalously high (~3×) for mixed-valence RFe_2O_4 ferrites compared with $LuFeCoO_4$ (see Table I). This provides direct evidence that the triangular basis of the FeO_5 bipyramids is distorted in the mixed-valence ferrites due to the presence of a mixed-valence state for the Fe atom. We estimate the maximum distortion in the equatorial plane to be about 0.1 Å.

The temperature dependence of the EXAFS spectra has been also studied in these mixed-valence RFe_2O_4 (R = Lu,Y,Yb) samples. The modulus of the FT of the k-weighted EXAFS spectra for the polycrystalline samples at different temperatures is displayed in Fig. 9. The very weak temperature dependence of the intensity of the first oxygen shell indicates nearly the same distortion of the FeO_5 bipyramids in the temperature range studied for each of the samples. However,

TABLE I. Best fit structural parameters for the first and second coordination shells of RFe_2O_4 (R = Lu,Y,Yb) and $LuFeCoO_4$ at the Fe K-edge. Contributing paths with the coordination number N from crystallography are indicated, where //**c** and ⊥**c** subscripts stand for contribution mainly along the hexagonal c axis direction and perpendicular to it, respectively. Average interatomic distances R and Debye-Waller factors σ^2 are given for each path. Numbers in parentheses are the errors estimated from different analyses to the best significant digit.

	$LuFe_2O_4$		YFe_2O_4		$YbFe_2O_4$		$LuCoFeO_4$[a]	
Path (× N)	R (Å)	σ^2 (Å^2)	R (Å)	σ^2 (Å^2)	R (Å)	σ^2 (Å^2)	R (Å)	σ^2 (Å^2)
Fe-$O_{//c}$ (× 2)	1.96 (3)	0.013 (2)	1.93 (1)	0.014 (1)	1.97 (2)	0.017 (3)	1.95 (3)	0.012 (2)
Fe-$O_{\perp c}$ (× 3)	1.96 (1)	0.015 (4)	1.92 (1)	0.013 (1)	1.96 (1)	0.015 (3)	1.93 (1)	0.005 (1)
Fe-$Fe_{//c}$ (× 3)	3.12 (2)	0.012 (1)	3.06 (2)	0.015 (2)	3.11 (1)	0.012 (1)	3.11 (2)	0.012 (1)
Fe-$Fe_{\perp c}$ (× 6)	3.44 (1)	0.019 (1)	3.42 (5)	0.024 (2)	3.46 (1)	0.017 (1)	3.43 (2)	0.010 (1)
Fe-$R_{//c}$ (× 3)	3.58 (1)	0.013 (1)	3.69 (4)	0.011 (5)	3.60 (1)	0.018 (3)	3.59 (1)	0.009 (1)

[a]For the $LuFeCoO_4$ compound (R = Lu), Fe and Co ions occupy the same site with occupancy 1:1; therefore, the indicated Fe neighbors can be either Fe or Co.

the intensity of the second coordination shell peaks continuously decreases with increasing temperature for $LuFe_2O_4$ and $YbFe_2O_4$ compounds, while in the case of YFe_2O_4, a clear discontinuity is observed at temperatures close to the CO transitions. Since there are no significant changes in the position of the FT peaks with T either, the experimental data have been fitted, keeping the interatomic distances at the values found in the best fits at room temperature (see Table I) and refining only the σ^2 factors. Figure 10 shows the σ^2 factors of the Fe-O and Fe-Fe interatomic distances as a function of temperature crossing the CO phase transitions for $LuFe_2O_4$, YFe_2O_4, and $YbFe_2O_4$. In the case of $LuFe_2O_4$ and YFe_2O_4, the measurements were carried out in the oriented samples, and the data are divided into the contributions parallel and perpendicular to the c axis. For $YbFe_2O_4$, only the polycrystal sample was measured, and the first oxygen shell was fitted with a single average distance. Let us summarize the main results from the fits: the σ^2 of the Fe-O first shell distances remain nearly constant as a function of temperature in $LuFe_2O_4$ (both apical and equatorial oxygen atoms) and $YbFe_2O_4$ (the variation is less than 4%), whereas the temperature dependence of the σ^2 of the Fe-O first shell distances for YFe_2O_4 shows very weak anomalies coincident with the structural phase transitions, as shown in Fig. 10. These variations are more pronounced for the equatorial than for the apical oxygen atoms. Regarding the σ^2 of the Fe-Fe second shell distances, a similar behavior is found. For $LuFe_2O_4$ and $YbFe_2O_4$, a weak monotonous decrease with increasing temperature is reported, as expected from contributions of thermal vibrations. On the other hand, for YFe_2O_4, the thermal evolution of the

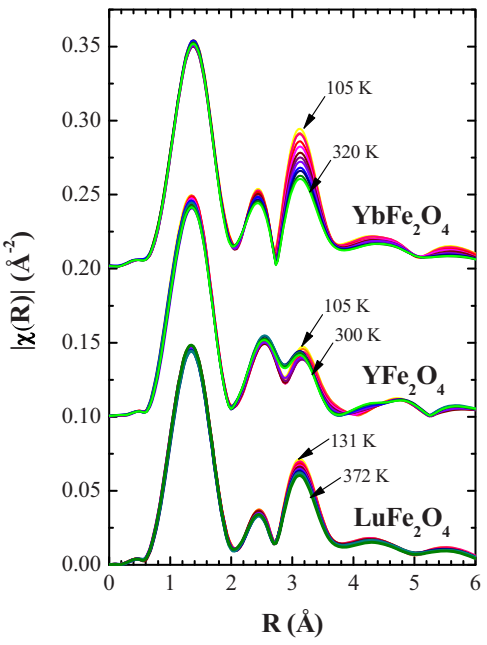

FIG. 9. (Color online) Temperature dependence of the moduli of the FTs of the $k\chi(k)$ EXAFS signals for the polycrystalline sample of $LuFe_2O_4$, YFe_2O_4, and $YbFe_2O_4$. Data at the minimum and maximum temperatures are indicated by an arrow in the figure with the corresponding temperature values, being the temperature variation among measurements of about 15 K.

σ^2 factors of the Fe-Fe distances also shows a discontinuity at around T_{CO}, stronger for the equatorial Fe atoms (Fig. 10). Finally, the σ^2 of the Fe-R distance (R = Lu,Y,Yb) increases continuously with temperature for the three compounds (not shown). These results indicate that the local distortion of the FeO_5 bipyramids is almost temperature-independent in the whole temperature range measured here and that the CO phase transitions measured by diffraction and DSC macroscopic techniques are due to the loss of coherence in the ordering of these distortions on heating above T_{CO} (i.e., they are mainly of order-disorder character).

In order to go further at resolving small structural changes in either interatomic distance R_j or σ_j^2 at the CO transition in YFe_2O_4 beyond the sensitivity of the previous analysis, we have evaluated the differential EXAFS signals (DEXAFS) obtained from subtraction between pairs of $k^2\chi(k)$ EXAFS spectra measured at consecutive temperatures. We have chosen for this analysis the sample YFe_2O_4, where a large variation in the σ^2 factors is obtained. As expected, the maximum variation observed in the DEXAFS signals corresponds to the spectra at temperatures just above and below the CO phase transition (see Fig. 11), showing a signature of the structural change. The FT of the differential signals (not shown) show peaks corresponding to both the oxygen first coordination shell and the Fe, Y, and O second shell. Therefore, the phase transition is also driven by the motion of atoms beyond the oxygen first coordination shell. In order to estimate the magnitude of the structural changes, we have followed the procedure given previously by Ruffoni *et al.* [54], noting that the method can only be applied separately to a single shell contribution. Therefore, we have estimated the changes associated with the first coordination shell by comparing the maximum DEXAFS signal with the original EXAFS at one selected temperature. Between high- and low-temperature–averaged EXAFS spectra, we obtain variations in the Fe-O interatomic distance and σ^2 factor of $\Delta R_{\text{Fe-O}} \sim 0.01$ Å and $\Delta\sigma^2{}_{\text{Fe-O}} \sim 0.001$ Å^2 for the $\mathbf{E}\perp\mathbf{c}$ data and $\Delta R_{\text{Fe-O}} \sim 0.005$ Å and $\Delta\sigma^2{}_{\text{Fe-O}} \sim 0.0006$ Å^2 for **E//c** spectra. This result indicates that the main instability lies on the hexagonal plane in agreement with the results obtained from the conventional EXAFS analysis. Therefore, in general and even for YFe_2O_4, where the local structural changes at T_{CO} are more pronounced than for the other mixed-valence ferrites, the variation of the average local disorder and the Fe-O distance at the phase transition is very weak.

IV. DISCUSSION AND CONCLUSIONS

The present Fe K-edge XAS study has allowed us to get a unified picture of the electronic and local structure around the Fe atom in the RFe_2O_4 ferrites. First, the XANES spectral features among the three mixed-valence RFe_2O_4 (R = Lu,Y,Yb) compounds are very similar to each other, independent of the rare earth atom and temperature. Furthermore, they cannot be reproduced by the weighted addition 1:1 of reference spectra corresponding to Fe^{3+} and Fe^{2+} pure-valence states at any temperature, even below T_{CO}. Therefore, iron atoms in the RFe_2O_4 (R = Lu,Y,Yb) ferrites are in an intermediate mixed-valence state that changes dynamically in the hexagonal phase and remains fixed at low temperatures in the CO phase. Using this linear combination

fit method for XANES quantitative analysis, we have obtained that the maximum charge disproportionation among different iron atoms in the mixed-valence $R\mathrm{Fe_2O_4}$ is about 0.5 electrons (*i.e.* the distribution should be $\mathrm{Fe}^{2+\delta}$ with $0.25 < \delta < 0.75$ and not necessarily bimodal). This experimental result seems to contradict previous RXS studies [7,40] in $\mathrm{LuFe_2O_4}$ that were considered to support the existence of $\mathrm{Fe}^{2+}/\mathrm{Fe}^{3+}$ CO. Let us comment shortly on the limitations of the reported RXS analysis. Satellite reflections $(h/3, k/3, l/2)$ that appear in the low-temperature CO phase come from a strong nonresonant Thomson scattering plus the energy-dependent anomalous term. When the Thomson scattering is larger than the anomalous contribution, the intensity of the reflections (I_{hkl}) is well described by the linear interference between the Thomson scattering (F_0) and the real part of the anomalous Fe scattering factor $(F'(E))$; that is, $I_{hkl} = F_{hkl}^2 = F_0^2 \pm 2F_0F'(E)$ with $F'(E) = \alpha \times [f'[\mathrm{Fe}^{3+}](E) - f'[\mathrm{Fe}^{2+}](E)]$. Mulders *et al.* [40] do not determine either the Thomson scattering or the α parameter that is given by the CO model and the crystallographic structure. Otherwise, they fit these

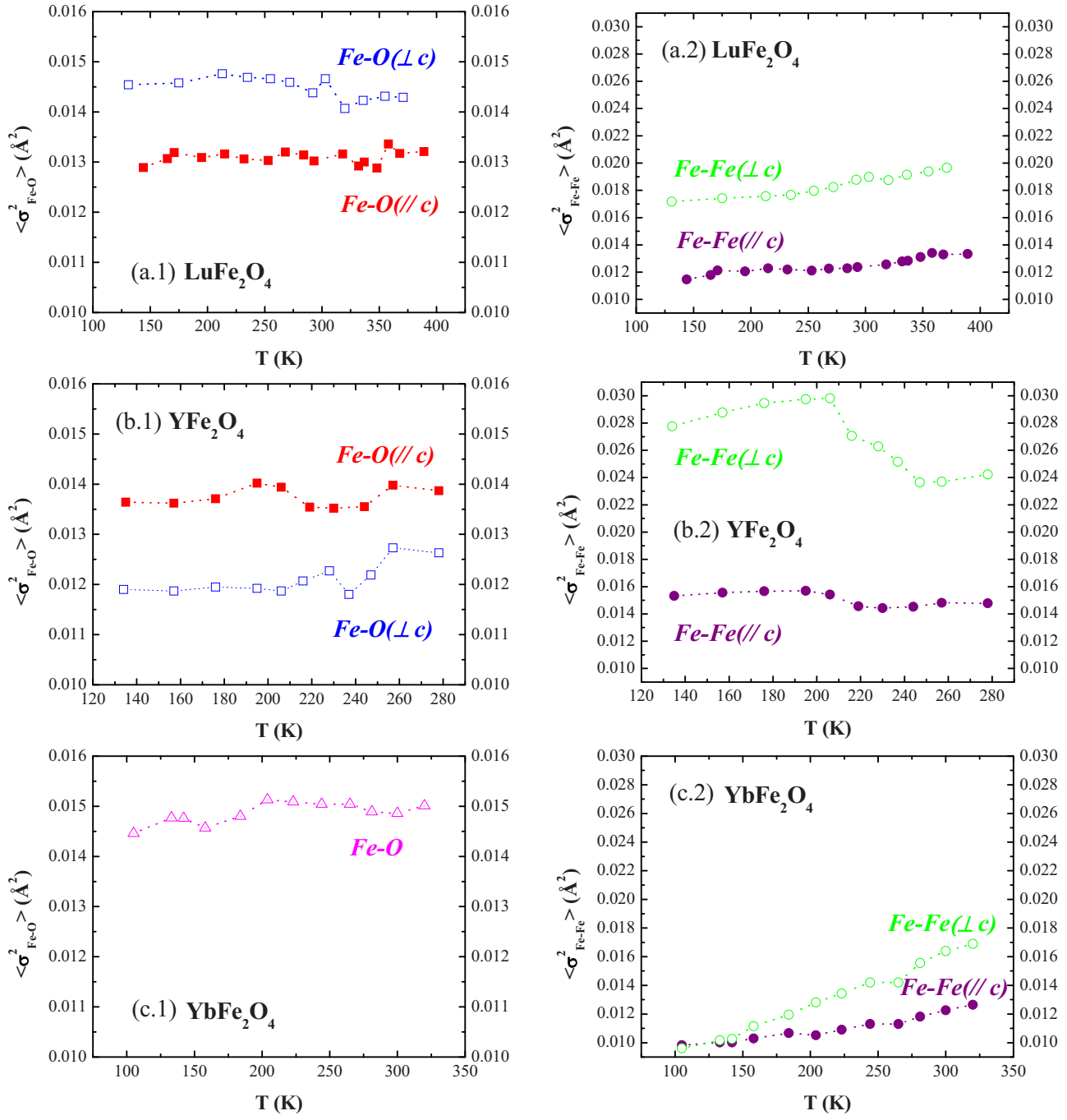

FIG. 10. (Color online) Thermal dependence of the refined Debye-Waller factors (σ^2) for the Fe-O and Fe-Fe distances of $\mathrm{LuFe_2O_4}$ and $\mathrm{YFe_2O_4}$ oriented samples and $\mathrm{YbFe_2O_4}$ polycrystal. //**c** and $\perp$**c** in parenthesis stand for contributions mainly along the hexagonal c axis direction and perpendicular to it, respectively.

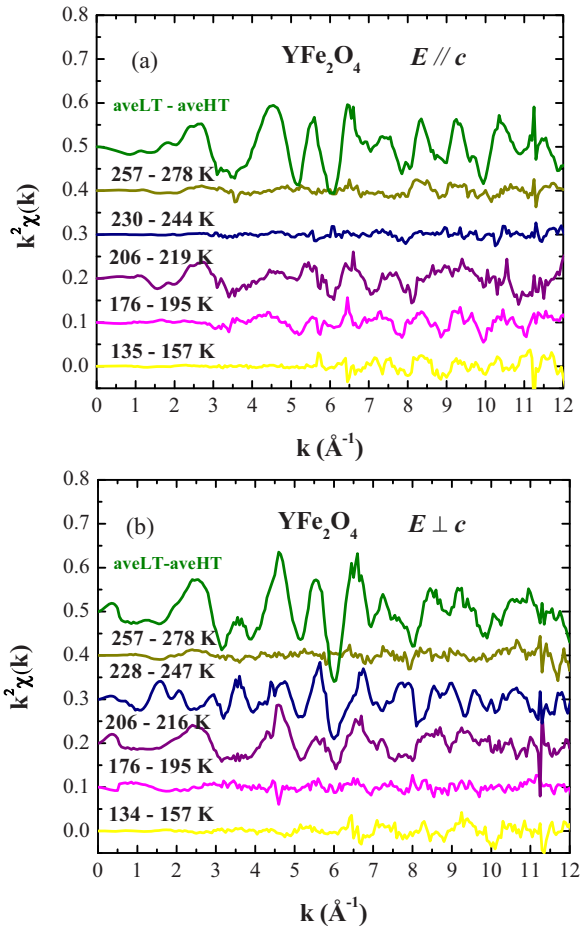

FIG. 11. (Color online) Differential EXAFS obtained for YFe_2O_4 oriented samples (a) **E//c** and (b) **E⊥c** from subtraction between pairs of EXAFS spectra measured at consecutive temperatures. The temperatures of the measurements subtracted are indicated for each difference in Kelvin units. Also, the difference between high- and low-temperature–averaged EXAFS spectra is shown.

two parameters as a unique parameter in their model and fix the chemical shift (charge disproportion). We note that a strong correlation exists between the chemical shift and the αF_0 term. In fact, the charge disproportion term can be written as $f'[Fe^{3+}](E) - f'[Fe^{2+}](E) = f'[Fe^{2.5+}](E + \Delta E) - f'[Fe^{2.5+}](E - \Delta E)$ and, when ΔE is small, as $f'[Fe^{3+}](E) - f'[Fe^{2+}](E) = \frac{df'[Fe^{2.5+}](E)}{dE} \times \Delta E$. Therefore, the same quality of the fit can be found with different ΔE values if the product $\alpha \cdot F_0$ is a free parameter. Summarizing, previous RXS studies have shown that charge segregation exists in the low-temperature CO phase, but it is impossible to determine the value of this charge segregation without a quantitative analysis including the structure factor of the exact CO sequence. Similar preliminary studies were shown in the past for manganites [55] that were later amended [56,57]. The occurrence of integer valence segregation in mixed-valence transition-metal oxides seems to be an exceptional fact, since the charge disproportionation associated with their CO transitions are generally small fractions of one electron [58].

The local structure around the Fe atoms in the mixed-valence RFe_2O_4 (R = Lu,Y,Yb) compounds is well described by a single average Fe-O distance with an anomalously high DW factor in the whole temperature range. The DW factor of each scattering path is the mean standard deviation of the average interatomic distance and includes contributions from both thermal vibrations and local distortions. The thermal vibration contribution decreases when lowering the temperature, so the presence of large DW factors in the low-temperature phase is a clear signature of the presence of local distortions. This average dispersion can originate from the presence of four distinct crystallographic sites for the Fe atom with slightly different average Fe-O distances, but the maximum distortion among them must be within the standard deviation given by the DW factor. The fact that a large DW factor is also obtained for the high-temperature undistorted phase indicates that the local environment around the Fe atom is also locally distorted, but dynamically and the structural transition is of order-disorder type. Polarized EXAFS data indicate that the obtained average Fe-O interatomic distances are nearly the same for the triangular basis within the *ab* plane and along the *c* axis of the FeO_5 bipyramid, which agrees with the fact that polarized XANES spectra does not show any significant chemical shift between the two **E//c** and **E⊥c** polarizations. The maximum distortion either in the *ab* plane or along the *c* axis resulting from the DW factor is found to be small ($\sim$ 0.1 Å). The lack of a strong distortion along the *c* axis of the bipyramid also applies to $LuFeCoO_4$ with only formal Fe^{3+} and it is a surprising result, which contrast to the strong apical distortion expected from the crystallographic hexagonal structure. On the other hand, $LuFeCoO_4$ shows a regular oxygen environment in the triangular basis of the bipyramid. Therefore, the CO transitions in the mixed-valence ferrites are mainly related to the distortions within the *ab* plane.

The absence of a ionic Fe^{3+}/Fe^{2+} segregation in the low-temperature CO phase for the three studied ferrites together with the order (static local distortions)-disorder (dynamic local distortions) character of the CO transitions agree with the Mossbauer studies on these samples [17,33]. These studies conclude that the iron atoms fluctuate between two charge states, which are neither 2+ nor 3+ in its literal meaning. In our description, the charge at the iron site fluctuates above T_{CO}, giving rise to a dynamical disproportion that is also followed by the local geometrical structure, and it is frozen at the iron sites below T_{CO}. The only question that remains open is whether the charge distribution is bimodal or multimodal, taking into account that the low-temperature phase of $LuFe_2O_4$ has the $C/2m$ monoclinic symmetry with four distinct iron sites, which suggests four different charged iron atoms [27].

Summarizing, we can conclude that the iron atom in the hexagonal structure of the RFe_2O_4 compounds is highly unstable, the local structure being different from the average crystallographic structure. This local structure instability is consistent with a distribution of distorted bipyramids giving rise to an inhomogeneous distribution of local charges. When cooling down, these distortions become ordered, decreasing the crystal symmetry. The ordered sequence and the resulting symmetry of the low-temperature phase depend on the composition (type of R cation) and oxygen stoichiometry. In this way, for $LuFe_2O_4$ and YFe_2O_4, below T_{CO}, different

fractional charges are localized in the lattice giving rise to an ordered sequence of charges, and larger discontinuities are observed in the crystal structure. On the contrary, a random distribution [59] or an incommensurate ordering seems to occur for the $YbFe_2O_4$ compound [16], which remains in the hexagonal crystallographic structure even at low temperatures. Finally, the local structure instability should have an important role in the electrical properties, but their correlation with the kind of charge order is a matter of future studies.

ACKNOWLEDGMENTS

Financial support from the Spanish MINECO (Project No. MAT2012-38213-C02-01) and Diputación General de Aragón (DGA-CAMRADS) are gratefully acknowledged. We also acknowledge ALBA and SOLEIL for granting beam time, and we thank the CLAESS and SAMBA beam line staffs for their kind support. S.L. also thanks DGA for her research grant.

[1] V. A. M. Brabers, in *Handbook of Magnetic Materials*, edited by K. H. J. Buschow (Elsevier, Amsterdam, 1995), Vol. 8, and references therein.
[2] N. Kimizuka, E. Takayama-Muromachi, and K-Siratori in *Handbook on the Physics and Chemistry of Rare Earths*, edited by K. A. Gschneidner and L. Eyring (Elsevier, Amsterdam, 1990), Vol. 13, p. 283.
[3] K. F. Wang, J.-M. Liu, and Z. F. Ren, Adv. Phys. **58**, 321 (2009).
[4] M. Angst, Phys. Status Solidi RRL **7**, 383 (2013).
[5] K. Kato, I. Kawada, N. Kimizuka, and T. Katsura, Z. Kristallogr. **141**, 314 (1975).
[6] M. Isobe, N. Kimizuka, J. Iida, and S. Takekawa, Acta Crystallographica C **46**, 1917 (1990).
[7] N. Ikeda, H. Ohsumi, K. Ohwada, K. Ishii, T. Inami, K. Kakurai, Y. Murakami, K. Yoshii, S. Mori, Y. Horibe, and H. Kito, Nature (London) **436**, 1136 (2005).
[8] M. A. Subramanian, T. He, J. Chen, N. S. Rogado, T. G. Calvarese, and A. W. Sleight, Adv. Mater. **18**, 1737 (2006).
[9] M. Tanaka, J. Akimitsu, I. Inada, N. Kimuzuka, I. Shindo, and K. Siratori, Solid State Commun. **44**, 687 (1982).
[10] Y. Sakai, K. Kaneda, N. Tsuda, and M. Tanaka, J. Phys. Soc. Jpn. **55**, 3181 (1986).
[11] M. Kishi, S. Miura, Y. Nakagawa, N. Kimizuka, I. Shindo, and K. Siratori, J. Phys. Soc. Jpn. **51**, 2801 (1982).
[12] E. J. Verwey, Nature (London) **144**, 327 (1939).
[13] J. Blasco, J. García, and G. Subías, Phys. Rev. B **83**, 104105 (2011).
[14] G. Subias, J. Garcia, J. Blasco, J. Herrero-Martin, M. C. Sanchez, J. Orna, and L. Morellon, J. Synchr. Rad. **19**, 159 (2012).
[15] J. van den Brink and D. I. Khomskii, J. Phys.: Condens. Matter **20**, 434217 (2008).
[16] A. J. Hearmon, D. Prabhakaran, H. Nowell, F. Fabrizi, M. J. Gutmann, and P. G. Radaelli, Phys. Rev. B **85**, 014115 (2012).
[17] M. Tanaka, K. Siratori, and N. Kimizuka, J. Phys. Soc. Jpn. **53**, 760 (1984).
[18] A. M. Mulders, M. Bartkowiak, J. R. Hester, E. Pomjakushina, and K. Conder, Phys. Rev. B **84**, 140403(R) (2011).
[19] A. B. Harris and T. Yildirim, Phys. Rev. B **81**, 134417 (2010).
[20] K.-T. Ko, H.-J. Noh, J.-Y. Kim, B.-G. Park, J.-H. Park, A. Tanaka, S. B. Kim, C. L. Zhang, and S-W. Cheong, Phys. Rev. Lett. **103**, 207202 (2009).
[21] J. S. Wen, G. Y. Xu, G. Gu, and S. M. Shapiro, Phys. Rev. B **80**, 020403(R) (2009).
[22] H. J. Xiang and M.-H. Whangbo, Phys. Rev. Lett. **98**, 246403 (2007).
[23] A. Nagano, M. Naka, J. Nasu, and S. Ishihara, Phys. Rev. Lett. **99**, 217202 (2007).
[24] J. Rouquette, J. Haines, A. Al-Zein, P. Papet, F. Damay, J. Bourgeois, T. Hammouda, F. Dore, A. Maignan, M. Hervieu, and, C. Martin, Phys. Rev. Lett. **105**, 237203 (2010).
[25] T. Michiuchi, Y. Yokota, T. Komatsu, H. Hayakawa, T. Kuroda, D. Maeda, Y. Matsuo, S. Mori, K. Yoshii, N. Hanasaki, T. Kambe, and N. Ikeda, Ferroelectrics **378**, 175 (2009).
[26] K. Kuepper, M. Raekers, C. Taubitz, M. Prinz, C. Derks, M. Neumann, A. V. Postnikov, F. M. F. de Groot, C. Piamonteze, D. Prabhakaran, and S. J. Blundell, Phys. Rev. B. **80**, 220409(R) (2009).
[27] J. de Groot, T. Mueller, R. A. Rosenberg, D. J. Keavney, Z. Islam, J.-W. Kim, and M. Angst, Phys. Rev. Lett. **108**, 187601 (2012).
[28] J. de Groot, K. Marty, M. D. Lumsden, A. D. Christianson, S. E. Nagler, S. Adiga, W. J. H. Borghols, K. Schmalzl, Z. Yamani, S. R. Bland, R. de Souza, U. Staub, W. Schweika, Y. Su, and M. Angst, Phys. Rev. Lett. **108**, 037206 (2012).
[29] F. Wang, J. Kim, and Y.-J. Kim, Phys. Rev. B **80**, 024419 (2009).
[30] B. Fisher, J. Genossar, L. Patlagan, and G. M. Reisner, J. Appl. Phys. **109**, 084111 (2011).
[31] J. Wen, G. Y. Xu, G. D. Gu, and S. M. Shapiro, Phys. Rev. B **81**, 144121 (2010).
[32] M. Angst, R. P. Hermann, A. D. Christianson, M. D. Lumsden, C. Lee, M.-H. Whangbo, J.-W. Kim, P. J. Ryan, S. E. Nagler, W. Tian, R. Jin, B. C. Sales, and D. Mandrus, Phys. Rev. Lett. **101**, 227601 (2008).
[33] X. S. Xu, M. Angst, T. V. Brinzari, R. P. Hermann, J. L. Musfeldt, A. D. Christianson, D. Mandrus, B. C. Sales, S. McGill, J.-W. Kim, and Z. Islam, Phys. Rev. Lett. **101**, 227602 (2008).
[34] X. S. Xu, J. de Groot, Q.-C. Sun, B. C. Sales, D. Mandrus, M. Angst, A. P. Litvinchuk, and J. L. Musfeldt, Phys. Rev. B **82**, 014304 (2010).
[35] A. D. Christianson, M. D. Lumsden, M. Angst, Z. Yamani, W. Tian, R. Jin, E. A. Payzant, S. E. Nagler, B. C. Sales, and D. Mandrus, Phys. Rev. Lett. **100**, 107601 (2008).
[36] Y. Zhang, H. X. Yang, Y. Q. Guo, C. Ma, H. F. Tian, J. L. Luo, and J. Q. Li, Phys. Rev. B **76**, 184105 (2007).
[37] D. Niermann, F. Waschkowski, J. de Groot, M. Angst, and J. Hemberger, Phys. Rev. Lett. **109**, 016405 (2012).
[38] A. Ruff, S. Krohns, F. Schrettle, V. Tsurkan, P. Lunkenheimer, and A. Loidl, Eur. Phys. J. B **85**, 290 (2012).
[39] S. Lafuerza, J. García, G. Subías, J. Blasco, K. Conder, and E. Pomjakushina, Phys. Rev. B **88**, 085130 (2013).

[40] A. M. Mulders, S. M. Lawrence, U. Staub, M. Garcia-Fernandez, V. Scagnoli, C. Mazzoli, E. Pomjakushina, K. Conder, and Y. Wang, Phys. Rev. Lett. **103**, 077602 (2009).
[41] J. Garcia, G. Subias, V. Cuartero, and J. Herrero-Martin. J. Synch. Rad. **17**, 386 (2010).
[42] G. Subías, J. García, M. G. Proietti, and J. Blasco, Phys. Rev. B **56**, 8183 (1997).
[43] J. Blasco, B. Aznar, J. García, G. Subías, J. Herrero-Martín, and J. Stankiewicz, Phys. Rev. B **77**, 054107 (2008).
[44] G. Subías, J. Garcia, J. Blasco, M. C. Sanchez, and M. G. Proietti, J. Phys.: Condens. Matter **14**, 5017 (2002).
[45] G. Subías, J. García, and J. Blasco, Phys. Rev. B **71**, 155103 (2005).
[46] http://www.cells.es/Beamlines/CLAESS/.
[47] E. Fonda, A. Rochet, M. Ribbens, L. Barthe, S. Belin, and V. Briois, J. Synchr. Rad. **19**, 417 (2012).
[48] J. J. Rehr and R. C. Albers, Rev. Mod. Phys. **72**, 621 (2000).
[49] B. Ravel and M. Newville, J. Synchrotron Radiat. **12**, 537 (2005).
[50] Y. Joly, Phys. Rev. B **63**, 125120 (2001).
[51] N. Ikeda, J. Phys.: Condens. Matter **20**, 434218 (2008).
[52] M. Benfatto, C. R. Natoli, A. Bianconi, J. García, A. Marcelli, M. Fanfoni, and I. Davoli, Phys. Rev. B **34**, 5774 (1986).
[53] D. C. Koningsberger and R. Prins, *X-Ray Absorption: Techniques of EXAFS, SEXAFS and XANES* (Wiley, New York, 1988).
[54] M. P. Ruffoni, R. F. Pettifer, S. Pascarelli, A. Trapananti, and O. Mathon, J. Synchrotron Radiat. **14**, 421 (2007).
[55] Y. Murakami, H. Kawada, H. Kawata, M. Tanaka, T. Arima, Y. Moritomo, and Y. Tokura, Phys. Rev. Lett. **80**, 1932 (1998).
[56] J. García, M. C. Sánchez, J. Blasco, G. Subías, and M. G. Proietti, J. Phys.: Condens. Matter **13**, 3243 (2001).
[57] J. Herrero-Martín, J. Blasco, J. García, G. Subías, and C. Mazzoli, Phys. Rev. B **83**, 184101 (2011).
[58] G. Subías, J. García, J. Blasco, J. Herrero-Martín, and M. C. Sánchez, J. Phys.: Conf. Series **190**, 012085 (2009).
[59] S. Lafuerza, J. García, J. Blasco, and G. Subías, FEMS EUROMAT 2013, Sevilla (2013) (unpublished).